

Effect of Glass Forming Additives on Low-Activity Waste Feed Conversion to Glass

Miroslava Vernerová^{1,2}, Karolína Šušová¹, Martina Kohoutková¹, Jaroslav Kloužek^{1,2}, Petra Cincibusová^{1,2}, Pavel Ferkl³, Jose Marcial³, Pavel Hrna⁴, Albert A. Kruger⁵, Richard Pokorný^{1,2*}

¹ University of Chemistry and Technology Prague, Technická 5/1905, 166 28 Prague 6, Czechia

² Institute of Rock Structure and Mechanics of the Czech Academy of Sciences, V Holesovickách 41, 182 09 Prague 8, Czechia

³ Pacific Northwest National Laboratory, Richland, WA 99354, United States of America

⁴ AttainX, Support Services Contractor to the Office of River Protection, U.S. Department of Energy, Richland, WA, USA

⁵ U.S. Department of Energy, Office of River Protection, Richland, WA 99354, U.S.A.

*Corresponding author: Richard.Pokorny@vscht.cz

Abstract

A significant effort was invested in the past to develop and refine mathematical models that relate the composition of nuclear waste glasses with their properties, such as viscosity, electrical conductivity, or chemical durability. However, less attention has been paid to the formulation of the melter feed itself, such as the chemical form and the particle size of the glass forming and modifying additives, which have a significant effect on the feed-to-glass conversion process during melting. To address this issue, we systematically changed the mineral composition of a simulated low-activity waste melter feed and inspected its melting behavior. When substituting minerals with corresponding oxides and hydroxides, we found that different alumina sources (kyanite, gibbsite, boehmite, or corundum) had the strongest effect on the feed melting process, whereas the sources of Ca, Mg, and Zr had little effect. The X-ray diffraction analysis showed that the alumina sources differ in their dissolution kinetics: early dissolving alumina sources, such as gibbsite ($\text{Al}(\text{OH})_3$) and boehmite ($\text{AlO}(\text{OH})$), increase the transient glass-forming melt viscosity at early stages, when gases still evolve, causing extended foaming, whereas alumina sources that dissolve at high temperatures, such as kyanite (Al_2SiO_5) and corundum (Al_2O_3), keep the transient glass-forming melt viscosity low and lead to a faster foam collapse. Using a viscosity-composition relationship to estimate the viscosity of transient glass-forming melts in the primary foaming range, we found that the primary foam began to collapse at 360 to 800 Pa s, and fully collapsed between 65 and 260 Pa s. This result agrees with our previous studies, according to which, the glass-forming melt viscosity at the cold cap foam bottom ranged from 24 to 85 Pa s.

Keywords: Glass melting; Vitrification; Nuclear waste; Glass-forming additives

1. Introduction

At the Hanford site in southeastern Washington, U.S., nearly 210,000 m³ of nuclear waste, generated during 45 years of plutonium production, is stored underground. The tank waste will be separated into low-activity waste (LAW) and high-level waste (HLW) fractions; both fractions will be mixed with glass-forming and -modifying additives, and vitrified using electric melters operated at ~1150 °C in the Waste Treatment and Immobilization Plant (WTP) [1-4]. Due to the continuous improvements and modifications to the WTP flowsheet, such as the bypass of the waste pretreatment facility [5-7], robust methods for the design of melter feeds and glass compositions are of primary importance.

The chemical composition of waste melter feeds is mainly formulated based on requirements for their high waste loading, chemical durability, melt viscosity, electrical conductivity, technetium retention, and melting rate [8-12]. In the last decades, a large body of research has been focused on designing advanced glass formulations that meet or exceed all the baseline requirements [13, 14]. The result of this effort is the development of partial quadratic mixture or machine learning models designed to predict the constrained properties as functions of glass composition [7, 15, 16]. These models have been validated and successfully used for designing advanced glass formulations with increased waste loading. However, one important process parameter received less attention – the melting rate. Without a general tool to support the optimization of feed formulation with respect to melting rate, the only source of melting rate data are expensive laboratory- and/or pilot-scale melter tests [17].

Because of the large amount of waste stored at Hanford, the need for high and stable waste throughput rates will increase as the WTP will start the operations [5]. Because the waste throughput rate is directly proportional to the melting rate, melting rate is of the primary concern during the vitrification of radioactive wastes. The options to achieve increased steady-state melting rates are limited to changing the melter operating temperature [18], changing the gas flow rate from bubblers [19], and changing the feed composition. The compositional changes include modifications that do not affect final glass composition (changing the additions of organic reductants, changing the mineralogical sources of glass-forming additives, and adjusting their granularity), but the overall process optimization may include changes leading to a modified glass composition [20, 21].

The effects of increased temperature and bubbling rate are significant and well understood. They are limited by restrictions stemming from the materials used (Inconel[®] melter electrodes cannot withstand long-term exposure to temperatures higher than ~1200 °C [22, 23]) and by the occurrence of undesirable phenomena, such as increased carry-over of particulates into off-gas, splashing of the feed, or decreased bubbling efficiency by jetting of the gas bubbles [24]. But there is presently no tool or model that could estimate the melting rate based on given feed composition, the effect of which on the steady-state melting rate is highly complex.

The melter feed design is a multi-dimensional problem. Our previous attempts to correlate the melting rate with the feed composition were thwarted by extremely high errors that made the values of correlation parameters meaningless. However, as recapitulated in Section 2, the recently developed melting rate correlation equation [25], which followed by the development of a detailed cold cap model [26-28] coupled with a cold cap-melter model of an electric waste glass melter [29, 30], showed that the rate of melting depends not only on the melter operation parameters, such as the melter operating temperature or

bubbling rate, but also on feed and glass properties: (i) the temperature at the cold cap bottom T_B [31], (ii) the conversion enthalpy ΔH [32], and (iii) the viscosity at the melter operating temperature η_{MO} [33]. These recent developments allow the estimation of the melting rate of any particular feed by using simple laboratory measurements. Nevertheless, there is currently no link between the melter feed composition and these properties. If we were now asked to improve the melting rate of a given feed by changing its design, we would make an educated guess, prepare samples, perform analyses to determine T_B and ΔH and after several iterations, come up with a recommendation.

To address this issue, as described in Section 3, we systematically changed the melter feed composition of a LAW melter feed by replacing mineral sources of glass-forming and modifying additives (GFMA), one at a time, with respective oxides while keeping the final glass composition unchanged and examined its melting behavior. The initial results presented in Section 4 show that the alumina sources had the most significant effect on the foaming and thus the conversion process. To understand the effect of alumina sources, we performed an X-ray diffraction analysis (XRD), which revealed significant differences in their dissolution kinetics. In Section 5, we used a viscosity-composition relationship to evaluate the effect of the different alumina sources on the transient glass-forming melt viscosity, and analyzed its relationship to the feed melting behavior, such as foam onset and foam maximum temperature.

This work is the first step in the development of a tool that could guide the process of the selection of glass forming and modifying additives (GFMA's), i.e., selection of chemical or mineralogical form of components, particle size, etc., that would have the largest impact on the melting rate, saving expensive and time-consuming laboratory work and/or improving the recommendations. This work is inspired by our previous work of changing individual components (iron and alumina sources) in HLW glasses [17], but extends it to testing all minerals and chemicals typically added to LAW melter feeds.

2. Theory

The glass production rate of LAW melter feeds can be estimated as a function of the geometrical and operational parameters of the melter, the physical properties of final glass, and the properties of melter feed through the melting rate correlation (MRC) equation [34]:

$$j = \xi_1 \left(\frac{h u_B \rho}{\eta} \right)^\gamma \frac{T_{MO} - T_B}{\Delta H} \quad (1)$$

where h is the melt pool depth, u_B is the bubbling rate (volumetric flow rate per melt area), ρ is the melt density, η is the melt viscosity, T_{MO} is the melter operating temperature, T_B is the cold cap bottom temperature, ΔH is the conversion enthalpy, and ξ_1 and γ are fitting coefficients. Parameters $\xi_1 = 459 \text{ Wm}^{-2}\text{K}^{-1}$ and $\gamma = 0.327$ were estimated by fitting Eq. (1) to a set of data from pilot-scale melter tests reported by Vitreous State Laboratory (VSL) [34].

The melt pool depth, the melter operating temperature, and the bubbling rate are set by the melter design and operations. Regarding the melt properties, mathematical models can be used to relate the melt viscosity to temperature and glass composition [9], and the melt density depends on the glass composition only weakly, so an average value of $\rho = 2600 \text{ kg m}^{-3}$ was chosen for all LAW glasses [34]. Next to the melter

operating conditions and melt properties, two variables affecting the melting rate depend on the melter feed formulation: the conversion enthalpy, ΔH , and the cold cap bottom temperature, T_B .

The enthalpy of conversion of melter feed to molten glass consists of sensible, reaction, and water evaporation enthalpies (ΔH_S , ΔH_R , and ΔH_W , respectively). The ΔH_R was measured using thermal gravimetry–differential scanning calorimetry, NETZSCH STA 449 F1, using a run-rerun method by integrating the heat flow over the temperature interval from room temperature to the T_{FO} [32]. The ΔH_W was computed using the reported slurry water content along with a known value of water evaporation enthalpy (2256 J g^{-1}). Finally, as discussed in [34-36], the ΔH_S can be estimated as $c_p(T_{MO} - T_{100^\circ\text{C}})$, where c_p is the average heat capacity (assumed to be 1.1 J K g^{-1} for all feeds). Fig. 1 displays the comparison of conversion enthalpies for a range of HLW and LAW feeds, considering $T_{MO} = 1150 \text{ }^\circ\text{C}$ (the composition of these feeds can be found in Lee et al. [34]). Due to the high amount of water in the feed, the conversion enthalpy is in general dominated by ΔH_W . Because of their lower water content, LAW feeds generally melt faster than HLW feeds (the average $\Delta H = \sim 3000$ and $\sim 6000 \text{ J g}^{-1}$ for LAW and HLW feeds, respectively). The reaction heat, ΔH_R , is relatively small; for LAW feeds, it can be even negative because of the exothermic reactions between nitrates and organics. As a result, changing the chemical and/or mineralogical form of the individual glass-forming or -modifying oxides, while keeping the content of slurry water and feed organics and nitrates constant, will have little to no effect on the conversion enthalpy.

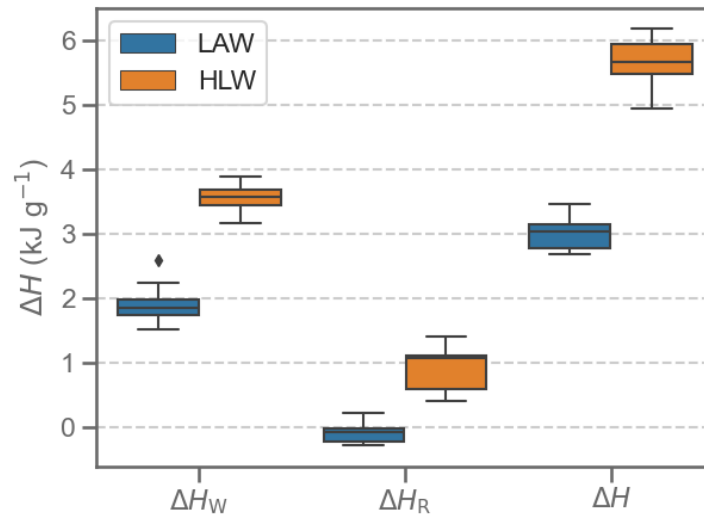


Fig. 1 Distribution of water evaporation, reaction, and total enthalpies (ΔH_W , ΔH_R , and ΔH , respectively) for a range of HLW and LAW melter feeds. The horizontal line represents the median, the box the middle 50 % of values and the notches the minimum and maximum values except for the outlier in HLW ΔH_W (shown as diamond). In that case the upper notch shows the highest value in the 1.5 times of the interquartile range. A constant value of sensible enthalpy $\Delta H_S = 1.16 \text{ kJ g}^{-1}$ was assumed for both HLW and LAW feeds.

Whereas $\Delta H = \Delta H_S + \Delta H_R + \Delta H_W$ is well defined and its estimation is relatively easy, evaluation of T_B is not as straightforward. By definition, the cold cap bottom temperature is that at which the primary foam collapses while the predominantly downward motion of the feed through the cold cap changes to predominantly horizontal motion of the melt circulating below the cold cap [37]. The choice of glass-forming or -modifying additives can significantly influence the primary foam collapse temperature by affecting both the gas evolution and the viscosity of the transient glass-forming melt, which determines the stability of the primary foam and defines the temperature at which the foam collapses [28, 33].

3. Experimental

3.1 Feed preparation

Table 1 lists the compositions of the nominal LAW simulant melter feed, which is based on the supernatant composition in Hanford LAW tank 241-AP-107 (AP-107) [38], and its modification, in which the main glass-forming and -modifying minerals were substituted with corresponding oxides and hydroxides to produce final glass of the same composition (Table 2). To investigate the effect of individual minerals and oxides/hydroxides on the melting characteristics, two feed series were prepared based on these nominal (with minerals) and oxides/hydroxide baseline compositions – minerals were substituted, one by one, into the oxides/hydroxide feed, and oxides were substituted, again one by one, into the nominal feed. Because varying the alumina sources in these feeds had the strongest effect on their foaming characteristics during melting, a third feed series was prepared, in which different alumina sources (gibbsite, boehmite, or corundum) and different particle size (kyanite with median particle size $d_{50} = 31 \mu\text{m}$ (nominal – coarse), $13 \mu\text{m}$ (medium), and $5 \mu\text{m}$ (fine), corundum with median particle size $d_{50} = 60 \mu\text{m}$ (coarse) and $d_{50} = 2 \mu\text{m}$ (fine)) were tested in the nominal AP-107 feed. Table 3 summarizes the three feed series tested.

Feeds were batched by adding the chemicals and minerals (in the order listed in Table 1) to deionized water while stirring [39]. The feed slurries were then partially dried using a hot plate at $90 \text{ }^\circ\text{C}$ before being fully dried in an oven at $105 \text{ }^\circ\text{C}$ overnight. Dry feeds were then crushed and sieved to a powder with a particle size below $100 \mu\text{m}$.

Table 1. Composition of simulated baseline LAW feeds, in grams per kilogram of glass produced

Melter feed	AP-107	AP-107
Baseline	nominal	oxides/hydroxide
Simulant	Mass (g)	
$\text{Al}(\text{NO}_3)_3 \cdot 9\text{H}_2\text{O}$	137.54	
$\text{Ca}(\text{NO}_3)_2 \cdot 4\text{H}_2\text{O}$	0.31	
$\text{Fe}(\text{NO}_3)_3 \cdot 9\text{H}_2\text{O}$	0.18	
NiO	0.04	
PbO	0.02	
NaOH	86.76	
KOH	5.38	
$\text{Na}_2\text{CrO}_4 \cdot 4\text{H}_2\text{O}$	2.34	
$\text{Na}_3\text{PO}_4 \cdot 12\text{H}_2\text{O}$	6.97	
NaCl	6.85	

NaF		0.91
Na ₂ SO ₄		7.87
NaC ₂ H ₃ O ₂		3.43
NaCHO ₂		3.74
Na ₂ C ₂ O ₄		0.96
NaNO ₂		77.23
NaNO ₃		70.33
Na ₂ CO ₃		57.39
GFMA*	Mass (g)	Mass (g)
H ₃ BO ₃	181.55	181.55
TiO ₂	14.92	15.00**
Li ₂ CO ₃	22.43	22.43
Mg ₂ SiO ₄	29.02	0.00
MgO	0.00	14.80
ZnO	35.95	35.95
ZrSiO ₄	45.80	0.00
ZrO ₂	0.00	30.20
Fe ₂ O ₃	56.47	59.31**
Al ₂ SiO ₅	71.26	0.00
Al(OH) ₃	0.00	63.40
CaSiO ₃	84.67	0.00
CaO	0.00	39.20
SiO ₂	370.07	469.27
C ₁₂ H ₂₂ O ₁₁	60.04	60.04
Total (g·kg ⁻¹ of glass)	1440.43	1459.40

*Glass-forming and -modifying additives

**The amounts of TiO₂ and Fe₂O₃ are slightly higher to account for their presence as impurities in wollastonite, kyanite, and olivine (forsterite)

Table 2. Glass composition of simulated LAW feeds in mass fractions

Glass oxide	Mass fraction
Al ₂ O ₃	6.09
B ₂ O ₃	10.03
Li ₂ O	0.90
Na ₂ O	16.97
SiO ₂	45.66
TiO ₂	1.40
Cr ₂ O ₃	0.07
ZrO ₂	3.01
CaO	3.95
Fe ₂ O ₃	5.52
MgO	1.49
ZnO	3.51
K ₂ O	0.38
Cl	0.41
F	0.04
P ₂ O ₅	0.13

SO ₃	0.43
NiO	0.004
PbO	0.002
Total	100.00

Table 3. Glass composition

Series I (AP-107 nominal)	Series II (AP-107 oxides/hydroxide)	Series III (AP-107 nominal)
Baseline nominal feed	Baseline oxides/hydroxide feed	Baseline nominal feed
– CaSiO ₃ / + CaO	– CaO / + CaSiO ₃	Al ₂ SiO ₅ (13 μm, 5 μm)
– Mg ₂ SiO ₄ / + MgO	– MgO / + Mg ₂ SiO ₄	– Al ₂ SiO ₅ / + Al(OH) ₃
– Al ₂ SiO ₅ / + Al(OH) ₃	– Al(OH) ₃ / + Al ₂ SiO ₅	– Al ₂ SiO ₅ / + AlO(OH)
– ZrSiO ₄ / + ZrO ₂	– ZrO ₂ / + ZrSiO ₄	– Al ₂ SiO ₅ / + Al ₂ O ₃ (60 μm, 2 μm)

3.2 High-temperature visual observation of melting

The characteristics of primary foaming were evaluated using a high-temperature visual observation of the feed-to-glass conversion during the feed expansion tests (FET) [40]. For FET, 1-g pellet samples, 13 mm diameter and ~6 mm thick (compressed at 28MPa for 2 min), are heated from room temperature to 1150 °C at 10 K min⁻¹, while their profile is monitored with a camera. From the profile area, the sample volume is evaluated by the method of cylinders of a trapezoidal cross-section, implemented in NIS Elements[®] software (Laboratory Imaging, Czech Republic). Integrated volumes were normalized to the final bubble-free glass melt volume, $V_G = (m_{\text{feed}}/\rho_{\text{glass}})(1 - \text{LOI})$, where LOI is the feed mass loss on ignition, m_{feed} is the feed mass, and $\rho_{\text{glass}} \approx 2.5 \text{ g cm}^{-3}$ is the molten glass density. FET experiments were performed in triplicate for error analysis. The foam onset temperature, T_{FO} , is obtained from FET as the temperature of minimal feed volume before feed expands due to foaming, while T_{FM} corresponds to the temperature of maximum foam volume.

3.3 X-ray diffraction

The fractions of undissolved crystalline phases were measured using XRD. About 5 g of powder feed samples were heated at 10 K min⁻¹ to temperatures between 100 °C and 1100 °C in 100 °C increments. After reaching the desired temperatures, samples were air quenched, ground in a planetary ball mill (Fritsch Pulverisette 6, 10 grinding balls 20 mm diameter, 4 min at 300 rpm), and crushed to under 100 μm grain size. Approximately 1 g samples were treated in the XRD diffractometer (PANalytical X'Pert³ Powder) using continuous scan type, 5 to 80° 2θ angular range, 0.04° step size, 115 s scan step, Cu Kα anode, 40 kV, 30 mA generator settings, PIXcel1D detector (Malvern), and a ring-shaped holder with internal diameter 27 mm at 25 °C. Rietveld refinement was carried out using Highscore Plus software and amorphous fractions were obtained using the external standard method with SiO₂-quartz as the standard [41, 42]. For all refined patterns, the weighted-profile R value, R_{wp} , was under 10 %. The uncertainty in the determination of the amount of amorphous phase was ± 1 wt.%.

4. Results

4.1 Feed expansion tests

Fig. 2 displays the normalized volume (V/V_G) of the feed pellets as a function of temperature, T . For illustration, displayed are also profile images of AP-107 nominal and oxide/hydroxide feed pellets captured at room temperature, at T_{FM} , and at 1050 °C (after the foam collapsed). As the feed is heated, liquid molten salt phase appears at a temperature as low as 200 °C [43-46], initially in the form of low-viscosity, highly mobile molten salts. As the temperature increases, other components start to melt, until enough transient glass-forming melt is produced and its viscosity becomes low enough to close the open porosity and trap evolving gases, leading to volume expansion of the sample – primary foaming. For the feeds investigated in this study, foam begins to grow at temperatures, T_{FO} , approximately between 650 and 700 °C. Based on EGA (see supplementary material), the main gases responsible for the primary foaming are NO and O₂ from the decomposition of nitrates and nitrites in the feed, and residual CO₂ from the reactions of organics and decomposition of carbonates (further details about gas evolution and primary foaming can be found in [31, 47]).

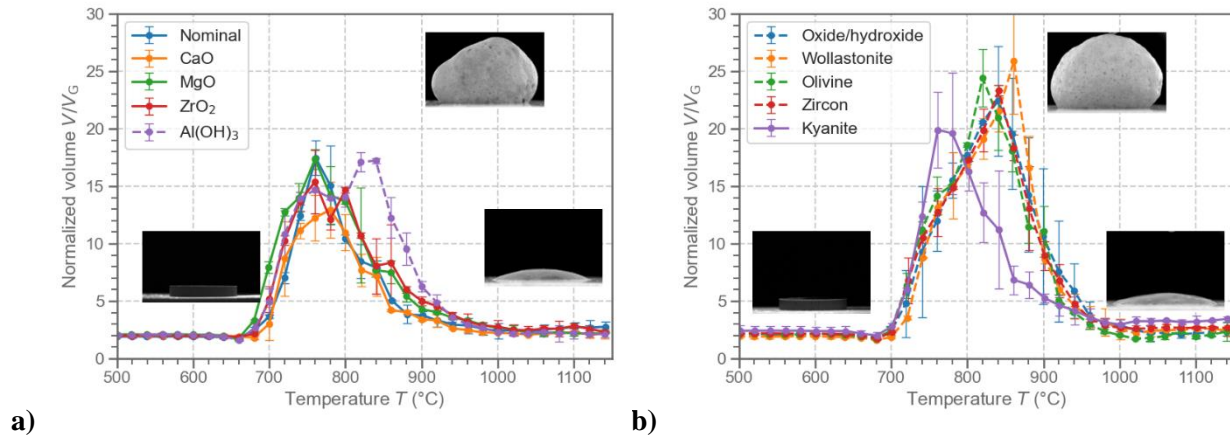


Fig. 2 Normalized volume of the feed as a function of temperature and composition: a) minerals baseline feed with substituted oxides/hydroxides, and b) oxides/hydroxide baseline feed with substituted minerals. Feeds containing Al₂SiO₅ as alumina source are displayed by solid lines, feeds with Al(OH)₃ by dashed lines.

As temperature increases above T_{FO} , the sample volume increases until it reaches its maximum volume, V_{FM} , at temperature T_{FM} (~750–900 °C), above which the volume decreases as primary foam gradually collapses. As discussed in Section 5, the T_{FM} value is closely related to the foam stability, defined by the transient glass-forming melt viscosity. As temperature further increases, residual gas evolving reactions, such as sulfate decomposition or ferric oxide reduction, can produce secondary bubbles that slow down the primary foam collapse observed during FET and can cause secondary maxima on the V/V_G profiles [31, 48]. A small gas phase fraction persists even at 1150 °C (removal of fine bubbles takes time [49-52]).

As displayed in Fig. 2a, changing the mineral sources of Ca (wollastonite), Mg (olivine – forsterite), and Zr (zircon) for their respective oxides had little effect on the position of foaming maxima ($T_{FM} \approx 750$ °C). However, changing the source of alumina (Al₂SiO₅ – kyanite) to Al(OH)₃ (gibbsite, a typical industrial

alumina source) lead to higher T_{FM} (Table 4), and the foam collapse occurred at higher temperature. A similar trend is observed in Fig. 2b – the sources of Ca, Mg, and Zr had little effect, but changing the source of alumina had a strong effect – the foam maximum and foam collapse in the feed with kyanite occurred at temperatures more than 100 °C lower when compared to the rest of the baseline oxides/hydroxide feeds containing $\text{Al}(\text{OH})_3$. Finally, Fig. 3 compares effects of different alumina sources and suggests that the particle size of kyanite does not affect the feed foaming behavior. Although T_{FO} is similar regardless of alumina source, boehmite and gibbsite exhibit higher T_{FM} values compared to kyanite and corundum. As explained in Section 5, the differences in foaming behavior of feeds with different alumina sources are caused by the differences in their dissolution kinetics, which significantly affects the viscosity of the transient glass-forming melt and thus the stability of the corresponding primary foam. The cold cap bottom temperature, T_B , was identified using evolved gas analysis (EGA) as detailed in the discussion section.

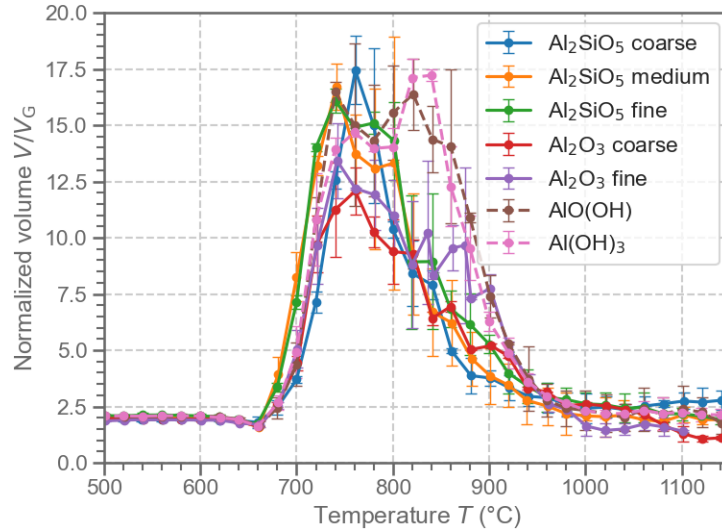


Fig. 3 Normalized volume (V/V_G) as a function of temperature for AP-107 feeds with varying alumina sources. Feeds containing Al_2SiO_5 and Al_2O_3 as alumina source are displayed by solid lines and feeds with other alumina sources by dashed lines.

Table 4. Foam onset, foam maximum, and foam bottom temperatures of melter feeds with varied alumina sources. Uncertainties of T_{FO} and T_{FM} were determined from multiple runs of FET. EGA, which was used for the determination of T_B , was performed only once.

Variant	T_{FO} (°C)	T_{FM} (°C)	T_B (°C)
Al_2SiO_5 coarse	652 ± 5	765 ± 1	850
Al_2SiO_5 medium	652 ± 1	760 ± 6	825
Al_2SiO_5 fine	652 ± 1	762 ± 4	850
Al_2O_3 coarse	654 ± 1	769 ± 4	910
Al_2O_3 fine	653 ± 1	767 ± 3	860
$\text{AlO}(\text{OH})$	656 ± 1	797 ± 2	930

4.2 Phase composition by X-ray diffraction

As the melter feed is heated, the primary melt contains inorganic salts, including nitrates, carbonates, sulfates, and perrhenates [46]. It has a low viscosity and is highly reactive. It reacts with borates in the feed to create early amorphous borate phase, which, in turn, starts to react with refractory solids. The XRD data for the AP-107 feeds with different alumina sources (full diffractograms are provided in Supplement S1), displayed in Fig. 4, suggest that the silica dissolution extent is almost identical in all feeds tested: silica starts to dissolve above 400 °C and reaches maximum dissolution rate at around 600 °C. However, as temperature further increases, the rate of silica dissolution decreases. This deviation from the ideal diffusion-controlled dissolution process is attributed to the inhibition of silica dissolution due to the irregular spatial distribution of silica particles; this is associated with the formation of nearly saturated melt on a large portion of their surfaces [53]. Other mineral components also gradually dissolve in the melt – gibbsite (Al(OH)₃) and zabuyelite (Li₂CO₃) by 300 °C, forsterite (Mg₂SiO₄) and anatase (TiO₂) by 500 °C, zincite (ZnO) by 600 °C, wollastonite (CaSiO₃) and hematite (Fe₂O₃) by 700 °C, and zircon (ZrSiO₄) by 1100 °C (trace amounts of zircon were still detected at 1100 °C). Regarding the different alumina sources, kyanite (Al₂SiO₅) and corundum (Al₂O₃) dissolve by ~900-1100 °C, depending on the particle size, and gibbsite dissolves by 300 °C, forming nano-crystalline Al₂O₃ (also referred to as “amorphous” because it is not detected by XRD). For the AP-107 feed with boehmite (AlO(OH)), the XRD patterns show the presence of trace amounts of boehmite below and at 300 °C, with majority transformed to nano-crystalline Al₂O₃ by 300 °C. As described in detail by Xu et al. [44], both gibbsite and boehmite in the melter feed thus initially follow similar thermal decomposition paths as pure Al(OH)₃ and AlO(OH), before the amorphous alumina starts to interact with alkaline oxides, borates, and silica, producing aluminoborate and aluminosilicate phases.

Crystalline salts were also detected. After the initial decrease in the concentration of NaNO₃, caused by its reaction with organics in the feed (mainly sucrose), its concentration increased as Al(NO₃)₃•9H₂O reacted with NaOH, forming NaNO₃. NaNO₃ was last detected at 600 °C, decomposing to gaseous NO_x and Na₂O that becomes a component of alkali-borate melt. Several intermediate crystalline phases, detected by XRD, precipitate during the conversion process or during sample cooling. For example, nitrate sodalite (Na₈(AlSiO₄)₆(NO₂)₂) is likely created around the dissolving silica particles. All crystalline solids eventually dissolve during the heating process or after a short residence time in the molten glass at 1100 °C.

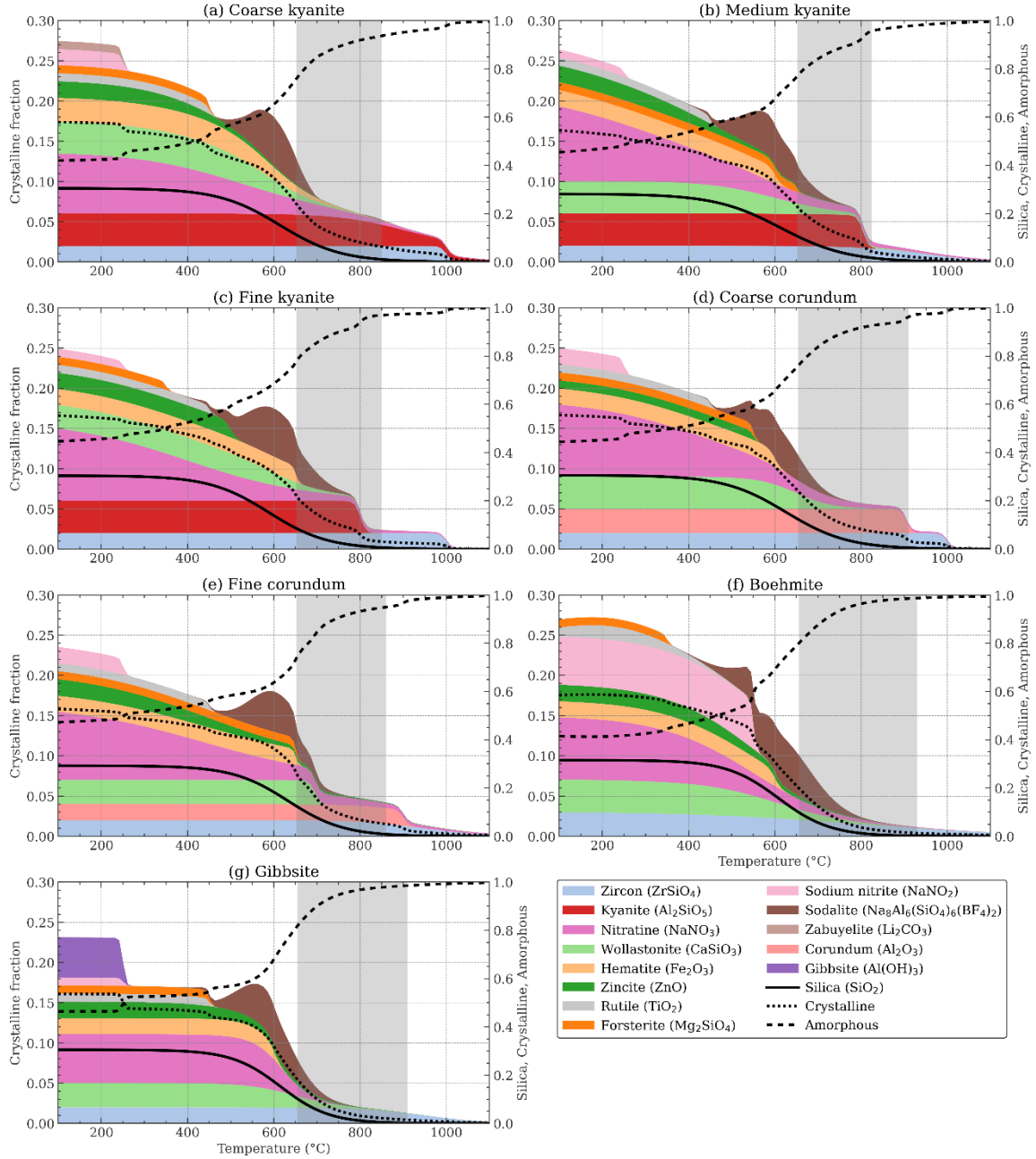


Fig. 4 Evolution of crystalline phases in AP-107 feed with varying alumina sources: a) nominal (coarse) kyanite (31 μm), b) medium kyanite (13 μm), c) fine kyanite (5 μm), d) coarse corundum, e) fine corundum, f) boehmite, and g) gibbsite. Fractions of silica as well as total amorphous and crystalline phases are plotted on right axes. Gray areas show foaming ranging from T_{FO} to T_B .

5. Discussion

The cold cap bottom is defined as a point where a predominantly vertical motion of the material within the cold cap turns to a predominantly horizontal motion of the circulating melt below, i.e., where the primary foam at the cold cap bottom collapses. The estimation of the cold cap bottom temperature from laboratory experiments is not straightforward because of the differences in the primary foam behavior in a heated batch sample during FET (where gases from collapsing primary foam can freely escape to the atmosphere) and at the bottom of a cold cap (where foam collapses internally until coalescing foam cells reach the size of gas cavities that move sideways, eventually escaping at the cold cap edge). However, both quenched cold caps from the laboratory-scale melter [54] and images from in-situ computed tomography [37, 55, 56] provide evidence that the mechanism of foam collapse is similar in both FET and at the cold cap bottom and that the foam collapse starts at the temperature of maximum foam volume. Thus, for low foaming feeds exhibiting fast foam collapse, the cold cap bottom temperature, T_B , can be generally identified as T_{FM} . However, the situation is different for feeds exhibiting extensive primary foaming, in which vigorous gas evolution continues even above T_{FM} , producing FET curves with very high, multiple, or flat foaming peaks. In that case, T_B , can be more precisely identified using evolved gas analysis (EGA) as a temperature (above T_{FM}) at which vigorous gas evolution stops [31].

As discussed by Lee et al. [33], the primary foam collapse is controlled by the foam stability that is, in the absence of surfactants, determined by the transient melt viscosity. Viscosity also affects the foam onset temperature – the minimum transient melt fraction needed for the melt to connect was found to increase by approximately 10 percent for each order of magnitude increase in the viscosity of the nascent melt [33].

By the augmented Adam-Gibbs model [57], the transient melt viscosity, η , can be estimated as

$$\ln\left(\frac{\eta}{\eta_\infty}\right) = \ln\left(\frac{\eta_g}{\eta_\infty}\right) \left(\frac{T_g}{T}\right) \left[s_{c0} - (s_{c0} - 1) \left(\frac{T_g}{T}\right)^f \right]^{-1} \quad (2)$$

where T is the temperature, T_g is the glass transition temperature, s_{c0} is the normalized configuration entropy of a depolymerized melt, and η_∞ , η_g , and f are constants (for LAW glasses, $\eta_\infty = 3.94 \times 10^{-6}$ Pa s, $\eta_g = 2.00 \times 10^{11}$ Pa s, and $f = 7.597$ [57, 58]). Composition-dependence of T_g and s_{c0} was modeled using a linear regression with coefficients reported by Ferkl et al. [57].

The temperature-dependent mass fractions of major components of the amorphous phase, virtually the transient glass-forming melt, is given by:

$$C_{ai} = \frac{g_i - \sum_{j=1}^M C_j c_{ij}}{1 - \sum_{j=1}^M C_j} \quad (3)$$

where C_{ai} is the i^{th} component mass fraction in the amorphous phase, g_i is the i^{th} component mass fraction in the final glass, C_j is the mass fraction of the j^{th} crystalline phase in the sample as detected by XRD, and c_{ij} is the i^{th} component mass fraction in the j^{th} crystalline phase; the sum is over all crystalline phases detected. Fig. 5 displays the glass-forming melt composition and Fig. 6 shows its fraction and viscosity as a function of temperature for the AP-107 feed with different alumina sources. Gibbsite and boehmite dissolve earlier than quartz, which leads to relatively high fractions of amorphous phase and high mass fractions of Al_2O_3 in the transient melt at T_{FO} and T_{FM} . As temperature increases, quartz and zircon continue to dissolve and dilute Al_2O_3 to its final fraction of 6.1% (Table 2). Corundum and kyanite dissolve later

than quartz, which leads to relatively low fractions of Al_2O_3 in the transient melt at T_{FO} and T_{FM} . This keeps the transient melt viscosity low and causes a faster foam collapse at lower amorphous phase fraction and lower cold cap bottom temperature T_B (see Table 1). According to the melting rate correlation, Eq. (1), using corundum and kyanite will thus lead to a higher rate of melting. Using fine kyanite or corundum leads to earlier dissolution, higher viscosities, and higher amount of amorphous fraction at given temperature compared to coarse variants. Nevertheless, factors other than melting rate determine the selection of the most suitable alumina source, such as the material availability and price, or the effect that the alumina source can have on other process parameters, such as the retention of radioactive technetium (recent studies suggest that the amorphous alumina that forms during the melting of feeds with gibbsite or boehmite can significantly increase Tc retention due to its high surface area [44, 46]).

Note that our findings are in agreement with previous studies investigating the effect of aluminum-containing raw materials on the melting of both nuclear waste feeds [17, 59] and industrial glass batches [60]. For example, both Pierce et al. [59] and Marcial et al. [17] reported that although gibbsite and boehmite dissolved below 500°C , corundum was still present in the waste glass feeds up to 900°C (irrespective of the corundum initial particle size); hence, the glass-forming melt lacked alumina in the batch with corundum. Similarly, Pavlyukevich et al. [60] investigated the effect of aluminum-containing raw materials on the melting of borosilicate e-glass fiber batches and concluded that the presence of $\gamma\text{-Al}_2\text{O}_3$ (amorphous alumina) accelerated the formation of aluminates and aluminosilicates and the melting of eutectic mixtures, increasing the conversion rate and reducing the energy consumption.

Naturally occurring aluminosilicates are typically used for commercial glass melting, such as feldspar or nepheline syenite, due to their availability, low costs, and fluxing behavior leading to melting acceleration and reduced melting energy when compared to pure Al_2O_3 [61]. Having a melting point between 1100 and 1250°C , these common minerals behave similarly to kyanite during glass melting. Other materials have been also considered and used, resulting in reduced melting temperatures and energy costs; these materials include minerals such as phonolite, obsidian, and sheridanite [62], or man-made blast furnace slag (calcium aluminosilicate by-product of iron production) [63, 64]. For more details, the reader is referred to a review by Bingham [61].

In comparison to the Al_2O_3 sources, changing the sources of CaO, MgO, or ZrO_2 (see Table 3) had little to no influence on foaming. Generally, this can be because: (i) their dissolution behavior is similar, and/or (ii) their effect on the viscosity of transient glass-forming melt is small. Considering that ZrO_2 strongly increases the viscosity, while CaO and MgO considerably decrease the viscosity of a typical waste glass melt, a likely explanation is that the dissolution behavior of the used Ca, Mg, and Zr sources was similar.

Similarly to our previous study [33], the results suggest that the minimum fraction needed for the melt to connect the open porosity at T_{FO} increases by $\sim 10\%$ for an order of magnitude increase in the transient glass-forming melt viscosity (see Fig. 6a and 6b). The viscosity at T_{FM} ranges within and 370 and 800 Pa s , respectively, which corresponds to ranges obtained in previous studies [28, 33]. Based on EGA data (see Supplementary S2), the cold cap bottom temperature, which is defined as temperature at which vigorous primary gas evolution stops and the primary foam collapses, ranges between 825 and 930°C . The corresponding transient melt viscosities range from 65 to 260 Pa s .

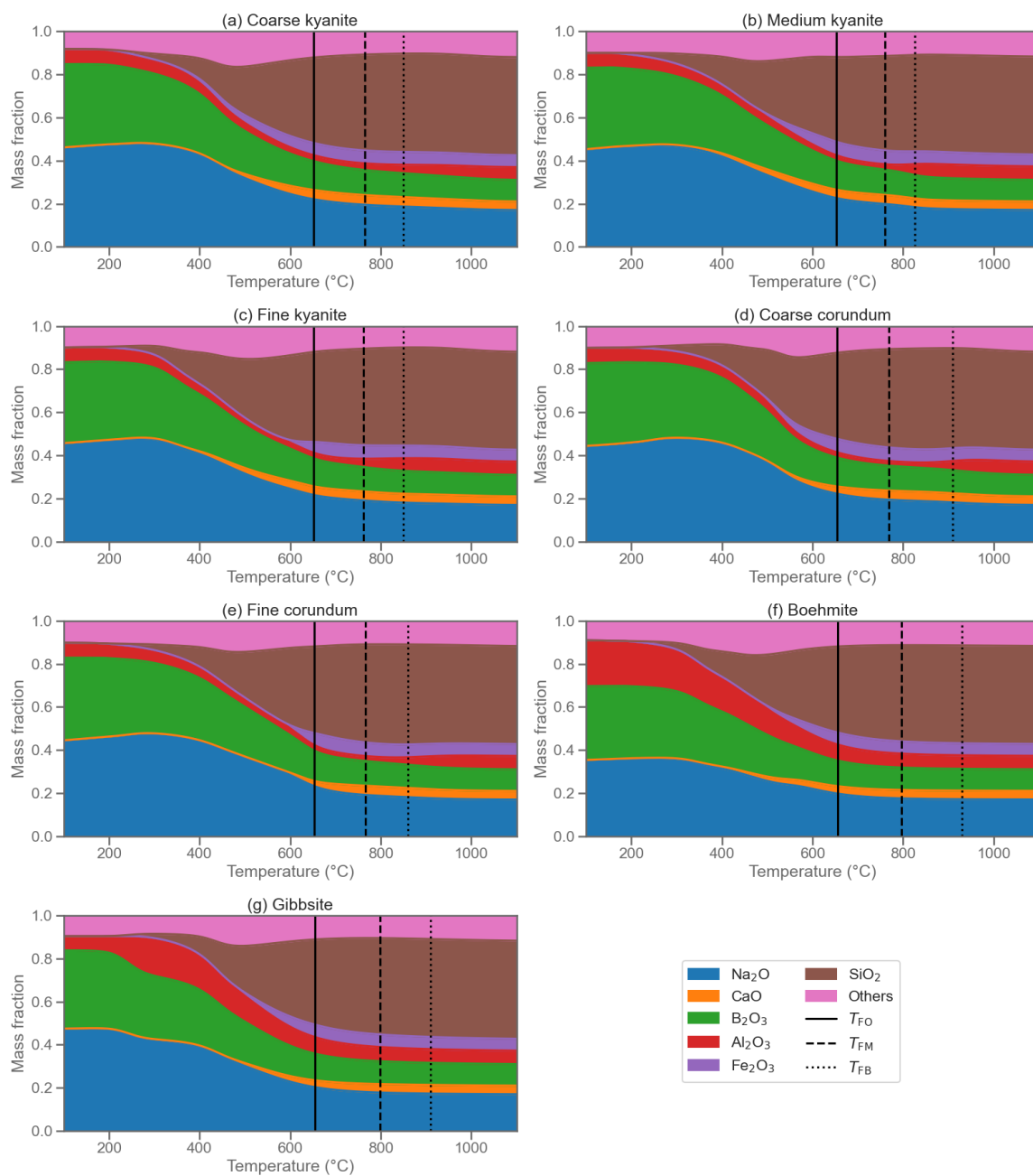


Fig. 5 Composition of amorphous phase versus temperature during melting of AP-107 feed with varying sources of alumina.

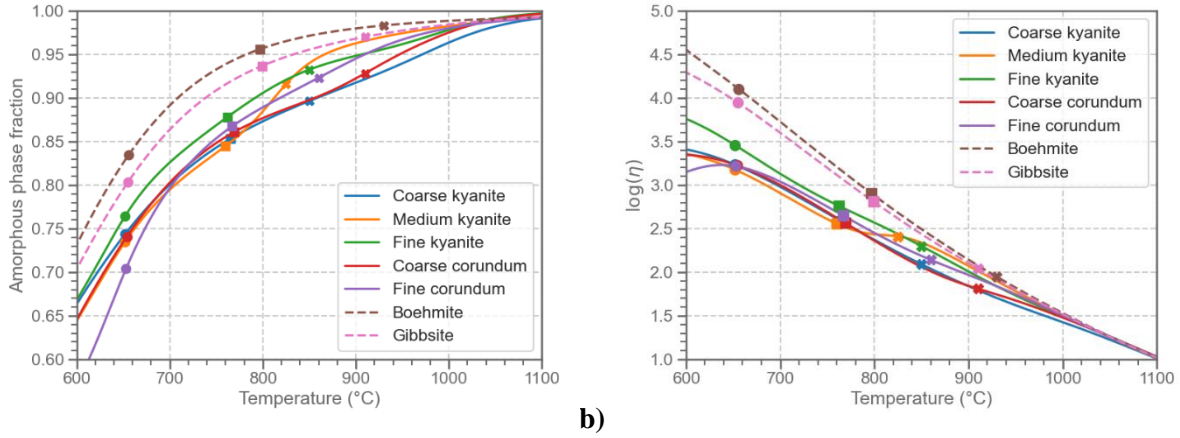


Fig. 6. Temperature dependence of a) transient melt viscosity for AP-107 feeds with varying alumina sources, calculated by Adam-Gibbs model, Eq. 2 [57] and b) amorphous phase fraction with respect to glass. The values at T_{FO} , T_{FM} , and T_B are marked by circles, squares, and crosses, respectively.

6. Conclusion

High-temperature visual observation was used to investigate the effect of chemical form and particle size of selected glass forming- and modifying-additives on the feed-to-glass conversion process. Whereas the different sources of Ca, Mg, and Zr had little effect on the melting process, different alumina sources resulted in different foaming behavior. By performing X-ray diffraction to evaluate the composition of transient glass-forming melt as a function temperature, we show that the differences in the conversion process can be explained by the differences in their dissolution kinetics:

- Feeds containing slowly-dissolving kyanite particles keep the transient glass-forming melt viscosity low and lead to a faster foam collapse.
- Feeds containing gibbsite and boehmite produce “amorphous” (nano-crystalline) Al_2O_3 , which significantly increases the transient glass-forming melt viscosity and shifts the foam maximum volume and foam collapse to higher temperatures.

Using the viscosity-composition relationship, we estimated the transient glass-forming melt viscosity at the onset of primary foam collapse to range from 360 to 800 Pa s, and that the foam fully collapsed between 65 and 260 Pa s, which is in good agreement with our previous results.

This work presents our first attempts to evaluate the effect of chemical form and particle size of glass forming- and modifying-additives on the waste glass melting process. The final goal of this work is to develop models that would relate the cold cap bottom temperature and the feed enthalpy to the feed composition, so that the melting rate correlation, Eq. (1), can be used to relate the glass production rate to the feed composition and thus to formulate feed makeup that maximizes it.

Acknowledgments

Jaroslav Kloužek, Miroslava Vernerová, Petra Cincibusová, and Richard Pokorný gratefully acknowledge financial support from the Czech Ministry of Education, Youth and Sports Project No.

LUAUS23062. The authors gratefully acknowledge the financial support provided by the U.S. Department of Energy (DOE) Waste Treatment and Immobilization Plant Project. Pacific Northwest National Laboratory is operated by Battelle for DOE under contract DE-AC05-76RL01830.

References

1. Pegg, I.L., *Turning nuclear waste into glass*. Physics Today, 2015. **68**(2): p. 33-39.
2. Matlack, K.S. and I.L. Pegg, *Advances in JHCM HLW Vitrification Technology at VSL through Scaled Melter Testing*, in *Advances in Materials Science for Environmental and Energy Technologies II*. 2013. p. 47-58.
3. Vienna, J.D., *Nuclear Waste Vitrification in the United States: Recent Developments and Future Options*. International Journal of Applied Glass Science, 2010. **1**(3): p. 309-321.
4. Colburn, H.A. and R.A. Peterson, *A history of Hanford tank waste, implications for waste treatment, and disposal*. Environmental Progress & Sustainable Energy, 2021. **40**(1): p. e13567.
5. Goel, A., et al., *Challenges with vitrification of Hanford High-Level Waste (HLW) to borosilicate glass – An overview*. Journal of Non-Crystalline Solids: X, 2019. **4**: p. 100033.
6. Marcial, J., et al., *Hanford low-activity waste vitrification: A review*. Journal of Hazardous Materials, 2024. **461**: p. 132437.
7. Lu, X., D.-S. Kim, and J.D. Vienna, *Impacts of constraints and uncertainties on projected amount of Hanford low-activity waste glasses*. Nuclear Engineering and Design, 2021. **385**: p. 111543.
8. Sargin, I., et al., *A data-driven approach for predicting nepheline crystallization in high-level waste glasses*. Journal of the American Ceramic Society, 2020. **103**(9): p. 4913-4924.
9. Ferkl, P., P. Hrma, and A. Kruger, *Parsimonious viscosity–composition relationships for high-temperature multicomponent glass melts*. Journal of Asian Ceramic Societies, 2022. **10**(1): p. 83-98.
10. Vienna, J.D., et al., *Glass Property-Composition Models for Support of Hanford WTP LAW Facility Operation*. 2022: United States.
11. Kim, D., *Glass property models, constraints, and formulation approaches for vitrification of high-level nuclear wastes at the US Hanford site*. Journal of the Korean Ceramic Society, 2015. **52**(2): p. 92-102.
12. Heredia-Langner, A., et al., *Hanford low-activity waste glass composition-temperature-melt viscosity relationships*. International Journal of Applied Glass Science, 2022. **13**(4): p. 514-525.
13. Marra, J.C. and D.-S. Kim, *Towards Increased Waste Loading in High Level Waste Glasses: Developing a Better Understanding of Crystallization Behavior*. Procedia Materials Science, 2014. **7**: p. 87-92.
14. James, C.M., et al., *Glass Formulation Development in Support of Melter Testing to Demonstrate Enhanced High Level Waste Throughput*. MRS Online Proceedings Library, 2008. **1107**(1): p. 231.
15. Vienna, J.D., *Compositional Models of Glass/Melt Properties and their Use for Glass Formulation*. Procedia Materials Science, 2014. **7**: p. 148-155.
16. Gunnell, L.L., et al. *Machine Learning with Gradient-Based Optimization of Nuclear Waste Vitrification with Uncertainties and Constraints*. Processes, 2022. **10**, 2365 DOI: 10.3390/pr10112365.
17. Marcial, J., et al., *Effect of Al and Fe sources on conversion of high-level nuclear waste feed to glass*. Journal of Nuclear Materials, 2022. **559**: p. 153423.
18. Pokorny, R. and P. Hrma, *Model for the conversion of nuclear waste melter feed to glass*. Journal of Nuclear Materials, 2014. **445**(1): p. 190-199.

19. Pokorny, R., A.A. Kruger, and P. Hrma, *Mathematical modeling of cold cap: Effect of bubbling on melting rate*. *Ceramics - Silikaty*, 2014. **58**(4): p. 296-302.
20. Lee, S., et al., *Effects of heating rate, quartz particle size, viscosity, and form of glass additives on high-level waste melter feed volume expansion*. *Journal of the American Ceramic Society*, 2017. **100**(2): p. 583-591.
21. Lee, S., et al., *Effects of alumina sources (gibbsite, boehmite, and corundum) on melting behavior of high-level radioactive waste melter feed*. *MRS Advances*, 2017. **2**(11): p. 603-608.
22. Vidensky, I., H. Gan, and I.L. Pegg, *Corrosion of Ni-Cr Alloys in Molten Salts and Hanford Low Waste Glass*, in *Environmental Issues and Waste Management Technologies in the Ceramic and Nuclear Industries VII*. 2006. p. 141-150.
23. Hsu, J.-H., et al., *Corrosion of Inconel 690 and Inconel 693 in an iron phosphate glass melt*. *Corrosion Science*, 2013. **75**: p. 148-157.
24. Guillen, D.P., et al., *Numerical comparison of bubbling in a waste glass melter*. *Annals of Nuclear Energy*, 2018. **113**: p. 380-392.
25. Lee, S., et al., *Glass production rate in electric furnaces for radioactive waste vitrification*. *Journal of the American Ceramic Society*, 2019.
26. Ueda, N., et al., *Conversion kinetics of container glass batch melting*. *Journal of the American Ceramic Society*, 2021. **104**(1): p. 34-44.
27. Ferkl, P., et al., *Model for batch-to-glass conversion: coupling the heat transfer with conversion kinetics*. *Journal of Asian Ceramic Societies*, 2021. **9**(2): p. 652-664.
28. Ferkl, P., et al., *Conversion kinetics during melting of simulated nuclear waste glass feeds measured by dissolution of silica*. *Journal of Non-Crystalline Solids*, 2022. **579**: p. 121363.
29. Abboud, A.W., D.P. Guillen, and R. Pokorny, *Effect of cold cap coverage and emissivity on the plenum temperature in a pilot-scale waste vitrification melter*. *International Journal of Applied Glass Science*, 2020. **11**(2): p. 357-368.
30. Abboud, A.W., et al., *Heat transfer from glass melt to cold cap: Computational fluid dynamics study of cavities beneath cold cap*. *International Journal of Applied Glass Science*, 2021. **12**(2): p. 233-244.
31. Hrma, P., et al., *Heat transfer from glass melt to cold cap: Gas evolution and foaming*. *Journal of the American Ceramic Society*, 2019. **102**(10): p. 5853-5865.
32. Chun, J., et al., *Cold-cap reactions in vitrification of nuclear waste glass: Experiments and modeling*. *Thermochimica Acta*, 2013. **559**: p. 32-39.
33. Lee, S.M., et al., *Viscosity of glass-forming melt at the bottom of high-level waste melter-feed cold caps: Effects of temperature and incorporation of solid components*. *Journal of the American Ceramic Society*, 2020. **103**(3): p. 1615-1630.
34. Lee, S., et al., *Melting rate correlation with batch properties and melter operating conditions during conversion of nuclear waste melter feeds to glasses*. *International Journal of Applied Glass Science*, 2021. **12**(3): p. 398-414.
35. Ferkl, P., et al., *Effect of material properties on batch-to-glass conversion kinetics*. *International Journal of Applied Glass Science*, 2023. **14**(4): p. 491-501.
36. Ferkl, P., et al., *Conversion degree and heat transfer in the cold cap and their effect on glass production rate in an electric melter*. *International Journal of Applied Glass Science*, 2023. **14**(2): p. 318-329.
37. Luksic, S.A., et al., *Through a glass darkly: In-situ x-ray computed tomography imaging of feed melting in continuously fed laboratory-scale glass melter*. *Ceramics International*, 2021. **47**(11): p. 15807-15818.

38. Matlack, K.S., et al., *DFLAW Glass and Feed Qualifications for AP-107 to Support WTP Start-Up and Flow-Sheet Development*, VSL-18R4500-1, Vitreous State Laboratory, The Catholic University of America, Washington, D.C. 2018.
39. Schweiger, M.J., et al., *Cluster formation of silica particles in glass batches during melting*. Journal of Non-Crystalline Solids, 2010. **356**(25): p. 1359-1367.
40. Hilliard, Z. and P. Hrma, *A Method for Determining Bulk Density, Material Density, and Porosity of Melter Feed During Nuclear Waste Vitrification*. Journal of the American Ceramic Society, 2016. **99**(1): p. 98-105.
41. McCusker, L.B., et al., *Rietveld refinement guidelines*. Journal of Applied Crystallography, 1999. **32**(1): p. 36-50.
42. Kemethmüller, S., et al., *Quantitative Analysis of Crystalline and Amorphous Phases in Glass–Ceramic Composites Like LTCC by the Rietveld Method*. Journal of the American Ceramic Society, 2006. **89**(8): p. 2632-2637.
43. Xu, K., et al., *Conversion of Nuclear Waste to Molten Glass: Cold-Cap Reactions in Crucible Tests*. Journal of the American Ceramic Society, 2016. **99**(9): p. 2964-2970.
44. Xu, K., et al., *Conversion of nuclear waste to molten glass: Formation of porous amorphous alumina in a high-Al melter feed*. Journal of Nuclear Materials, 2017. **483**: p. 102-106.
45. Nienhuis, E., M. Saleh, and J. McCloy, *Structural Characterization of Ternary Salt Melts for Low Activity Waste Applications*. MRS Advances, 2019. **4**(17): p. 1045-1056.
46. Pokorny, R., et al., *Transient melt formation and its effect on conversion phenomena during nuclear waste vitrification - HT-ESEM analysis*. Journal of the American Ceramic Society, 2023. **n/a**(n/a).
47. Appel, C.J., et al., *Effect of sucrose on foaming and melting behavior of a low-activity waste melter feed*. Journal of the American Ceramic Society, 2019. **102**(12): p. 7594-7605.
48. Lee, S.M., et al., *Heat transfer from glass melt to cold cap: Effect of heating rate*. International Journal of Applied Glass Science, 2019. **10**(3): p. 401-413.
49. Nemeč, L., *Refining in the Glassmelting Process*. Journal of the American Ceramic Society, 1977. **60**(9-10): p. 436-440.
50. Nĕmec, L., et al., *The semiempirical model of the multicomponent bubble behavior in glass melts*. Ceramics-Silikaty, 2012. **56**: p. 367-373.
51. Beerkens, R.G.C., et al., *Melting and Fining*, in *Mathematical Simulation in Glass Technology. Schott Series on Glass and Glass Ceramics (Science, Technology, and Applications)*. H. Loch and D. Krause, Editors. 2002, Springer: Berlin, Heidelberg, Germany.
52. Beerkens, R.G.C. and J. van der Schaaf, *Gas Release and Foam Formation During Melting and Fining of Glass*. Journal of the American Ceramic Society, 2006. **89**(1): p. 24-35.
53. Hrma, P. and J. Marcial, *Dissolution retardation of solid silica during glass-batch melting*. Journal of Non-Crystalline Solids, 2011. **357**(15): p. 2954-2959.
54. Dixon, D.R., et al., *Temperature Distribution within a Cold Cap during Nuclear Waste Vitrification*. Environmental Science & Technology, 2015. **49**(14): p. 8856-8863.
55. Luksic, S.A., et al., *In situ characterization of foam morphology during melting of simulated waste glass using x-ray computed tomography*. Ceramics International, 2020. **46**(11, Part A): p. 17176-17185.
56. Marcial, J., et al., *In-situ X-ray and visual observation of foam morphology and behavior at the batch-melt interface during melting of simulated waste glass*. Ceramics International, 2022. **48**(6): p. 7975-7985.
57. Ferkl, P., P. Hrma, and A.A. Kruger, *Augmented Adam-Gibbs model for glass melt viscosity and configuration entropy as functions of temperature and composition*. Journal of Non-Crystalline Solids, 2022. **595**: p. 121832.

58. Hrma, P., P. Ferkl, and A.A. Kruger, *Glass length: Workability and meltability of glass as a function of glass melt fragility*. *Journal of Non-Crystalline Solids*, 2022. **597**: p. 121931.
59. Pierce, D.A., et al., *Effect of Alumina Source on the Rate of Melting Demonstrated with Nuclear Waste Glass Batch*. *International Journal of Applied Glass Science*, 2012. **3**(1): p. 59-68.
60. Pauliukevich, Y., et al., *Effect of aluminum-containing raw materials on the melting of borosilicate glass for fiber*. *Ceramics International*, 2021. **47**(22): p. 31092-31098.
61. Bingham, P.A., *Design of New Energy-Friendly Compositions*, in *Fiberglass and Glass Technology: Energy-Friendly Compositions and Applications*, F.T. Wallenberger and P.A. Bingham, Editors. 2010, Springer US: Boston, MA. p. 267-351.
62. Jordan-Hernandez, R., et al., *Sheridanite: A new raw material for industrial glass*. *American Ceramic Society Bulletin*, 2005. **84**.
63. Marriott, N., et al., *Results of the successful introduction of Calumite into a green container furnace*. *Glass Technology - European Journal of Glass Science and Technology Part A*, 2007. **48**(6): p. 290-296.
64. Kuśnierz, A.A., et al., *Influence of the increased content of Calumite blast-furnace slag on the melting of sodium–calcium–silicate glass*. *Journal of Thermal Analysis and Calorimetry*, 2019. **138**(6): p. 4571-4583.